

Universal relations after GW170817

Zachary Carson,¹ Katerina Chatziioannou,^{2,3} Carl-Johan Haster,^{2,3} Nicolàs Yunes,^{4,5} and Kent Yagi¹

¹*Department of Physics, University of Virginia, Charlottesville, Virginia 22904, USA*

²*Canadian Institute for Theoretical Astrophysics,
60 St. George Street, Toronto, Ontario, M5S 3H8, Canada*

³*Center for Computational Astrophysics, Flatiron Institute, 162 5th Ave, New York, NY 10010*

⁴*Department of Physics, Montana State University, Bozeman, MT 59717, USA.*

⁵*Department of Physics and MIT Kavli Institute,*

(Dated: December 17, 2018)

The thermodynamic relationship between pressure and density (the equation of state) of supranuclear matter, accessible primarily in neutron stars, is critical to the study of such stars, and is one of the largest uncertainties in nuclear physics to date. The extraction of tidal deformabilities from the gravitational waveforms of binary neutron star merger events, such as GW170817, is a promising method of probing the nuclear structure. Previous studies have shown that approximately equation of state insensitive “binary Love universal relations” exist between symmetric and antisymmetric combinations of individual tidal deformabilities, which are difficult to be independently measured with second-generation gravitational wave interferometers. Similarly, another set of equation of state independent relations exist between individual neutron star parameters: moment of inertia (I), tidal deformability (Love number), and quadrupole moment (Q) - known as the “I-Love-Q universal relations.” Such universal relations allow the elimination of some tidal parameters from the list of model parameters, thus breaking degeneracies and ultimately reducing the uncertainty of the dominant tidal effect in parameter estimation. In this document, we explain how one can reduce equation of state variation for both binary Love and I-Love-Q universal relations, which helps to reduce systematic errors on the tidal measurement of binary neutron star mergers. We achieve this by restricting to only equations of state drawn from the 90% posterior constraint on pressure as a function of density, as derived by the LIGO Collaboration. We find an improvement in binary Love universality by a factor of $\sim 59\%$ for stars with a mass ratio of 0.75, and in I-Love-Q universality by factors of $\sim 50\%$. We end by comparing systematic errors on tidal measurement due to the equation of state variation with statistical errors and comment on whether one can safely use these universal relations with future gravitational wave observations.

I. INTRODUCTION

The dependence of pressure on density for supranuclear matter found primarily inside neutron stars (NSs) remains to be one of the largest mysteries in both nuclear physics and astrophysics. This internal structure of such stars, known as the equation of state (EoS), is exceedingly important, as it is the determining factor for many NS observables - such as the mass, the radius, and many more. Unfortunately, terrestrial experiments can only study the EoS up to the nuclear saturation density ($\rho_{\text{sat}} \approx 2.5 \times 10^{14} \text{ g/cm}^3$) [1–5], making NSs ideal laboratories for constraining ultra dense nuclear matter.

Independent measurements of NS observables can be used to constrain the nuclear EoS. For example, electromagnetic observations of the mass-radius relationship of NSs have been used to place limits on NSs [6–10]. However, these implications suffer from large systematic errors due to astrophysical mismodeling. Alternatively, the emission of gravitational waves (GWs) from binary NS merger events have proven to be a unique method of probing nuclear physics. During the early inspiral portion of the merger, the orbital separation is large enough that the effect of companion tidal fields is negligible. As the separation decreases through GW emission, tidal forces are magnified and the NSs deform from sphericity, altering the orbital trajectories; a relic which is directly

imprinted on the GW signal. This deformation is characterized by the *tidal deformability* Λ as the linear response of the NSs quadrupole moment Q_{ij} to the neighboring tidal field ε_{ij} .

In the case of binary NSs, each star becomes deformed via the process highlighted above, resulting in two highly correlated tidal parameters Λ_1 and Λ_2 entering in the gravitational waveform. Due to high correlations between the two parameters, independent extraction becomes very difficult at current interferometer sensitivities. *zc: cite?* Typically, these high correlations can be reduced by strategically reparameterizing the waveform template with new tidal parameters constructed from linear combinations of Λ_1 and Λ_2 . For example, utilizing the parameters $\tilde{\Lambda}$ and $\delta\tilde{\Lambda}$ [11, 12] which enter the GW waveform at different post-Newtonian (PN) orders (powers of the ratio between the orbital speed and the speed of light v/c^{2n}) partially mitigates these correlations.

Unfortunately, current detectors are only sensitive enough to accurately measure the dominant tidal parameter, $\tilde{\Lambda}$, known as the chirp deformability. Previous work by Yagi and Yunes [13] resolved this issue by finding approximately EoS-insensitive “binary Love universal relations” between symmetric and anti-symmetric combinations of tidal deformabilities $\frac{1}{2}(\Lambda_1 \pm \Lambda_2)$. This allows one to further break degeneracies between tidal

parameters, resulting in both (i) a decrease in uncertainty upon parameter extraction on the removal of one parameter from the model, and (ii) the ability to measure the secondary tidal parameter upon measurement of the first. This important work showed up to an order of magnitude improvement in parameter estimation through a simple Fisher analysis. Similar “I-Love-Q” universal relations [14] have been found between individual NS observables: quadrupole moment, moment of inertia, and tidal deformability; similarly allowing the removal of tidal parameters from the model list, and allowing an automatic determination of one observable through the measurement of another.

In this analysis, we aim to improve this important work by imposing the restrictions found on the EoS [15] derived from the recent binary NS merger observation, GW170817 [16]. By restricting to only EoSs which lie within the 90% credible region on pressure as a function of density found in [15], we repeat the analyses done in [13, 14] and show an increase in universality for both binary Love and I-Love-Q universal relations. In addition, we consider hybrid star EoSs seen in [17], which experience strong first-order transitions from hadronic matter to quark matter. These provide a departure from the nuclear matter relations considered here - providing valuable insight into them. Further, we estimate the viability of using improved universal relations on future GW detections by performing simple Fisher analyses to approximate when the statistical errors from parameter extraction become comparable to the systematic errors due to EoS variation in universal relations.

A. Executive Summary

In this paper we attempt to improve binary Love and I-Love-Q universal relations by imposing constraints on the EoS found by GW170817 [15, 16]. First, we generate two large samples of spectral EoSs [18], where we (i) impose the restriction that they must be drawn from GW170817s 90% credible posterior in pressure as a function of density, and (ii) don’t impose any restrictions for comparison purposes. Next, we follow the important works of [13] and [14] to show how the “constrained” set of EoSs show improved universality from both the previous works, and the “unconstrained” sample, shown by Fig. 4. In addition, we determine the degree to which hybrid star EoSs obey binary Love universal relations. Finally, through a simple Fisher analysis, we consider the value in improving universal relations by approximating when the statistical errors from parameter extraction become comparable to the systematic errors due to EoS variation in universal relations.

Upon use of the constrained set of EoSs, we find an improvement in binary Love universality by a factor of $\sim 59\%$ for stars with mass ratios of 0.75, and in I-Love-Q universality by factors of $\sim 50\%$, tabulated in Tab. III. We also find that binaries consisting of one massive hy-

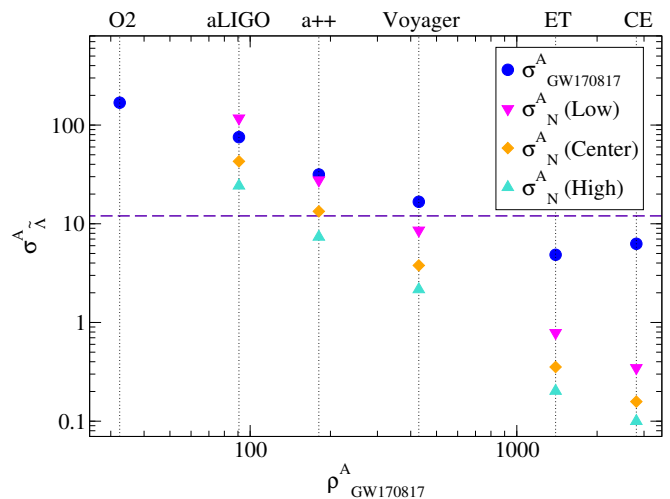


FIG. 1. Estimated statistical uncertainties $\sigma_{\text{GW170817}}^A$ (blue) in the extraction of $\tilde{\lambda}$ from GW170817 (O2) as if observed with future interferometers aLIGO, a++, Voyager, CE, and ET-D as a function of the signal-to-noise-ratio ρ_{GW170817}^A . This is compared to the combined uncertainty σ_N^A (red) from the observation of multiple events from a simulated population of size N_A corresponding to the upper (teal), central (orange), and lower (magenta) limits of expected binary NS merger detection rates for O2, aLIGO, a++, Voyager, CE, and ET-D over 1 observation year. It can be seen that the statistical errors in parameter extraction become comparable to the systematics from EoS variation in binary Love relations (purple) for Voyager and on. Note there is no simulated populations of events under the O2 design sensitivity - due to there only being a single event during the observing period. These results are further tabulated in Table VII.

brid star, and one small-mass hadronic star do not agree with derived binary Love relations, due to the large separation in $\tilde{\lambda}$ between the constituent stars. Unfortunately, due to the current limitations in detector sensitivity, the systematic errors arising from EoS variation in the universal relations are far outweighed by the statistical errors accrued by extraction of high-order PN tidal parameters from GW waveforms. Fig. 1 compiles the results from Fisher analyses approximating the uncertainties accrued from parameter extraction for GW170817 as if it had been observed by future detectors $A \equiv (\text{O2, aLIGO, a++, Voyager, ET, CE})$. Here, $\sigma_{\text{GW170817}}^A$ and ρ_{GW170817}^A correspond to the statistical error and signal-to-noise-ratio found from observing GW170817 on detector A , and σ_N^A represents the combined uncertainty after the detection of N_A events (corresponding to the binary NS merger rate associated interferometer A). These values are further tabulated in Table VII. It can be seen from this figure that the statistical errors from parameter extraction become comparable the universal relation systematics (indicated by the magenta horizontal line) for the Voyager telescope - indicating when improved binary Love universal relations will become viable.

The organization of this paper is outlined below. We begin with a complementary background and theory material in Sec. II. We continue in Sec. III by finding new and improved binary Love and I-Love-Q universal relations, and considering how well hybrid star EoSs agree with the universal relations. We next examine these improved universal relations and question whether or not they are useful for future interferometers in Sec. IV. We conclude in Sec. V by discussing our results and mentioning avenues of future work. Throughout this paper, we have adopted geometric units of $G = c = 1$, unless otherwise stated.

II. BACKGROUND AND THEORY

A. Spectral representations of neutron star equations of state

The structure of a NS and its tidal interactions in a binary system rely heavily on the underlying state function describing the relationship between pressure (p) and energy density (ϵ), or equation of state, of nuclear matter. Given that all currently proposed EoSs utilize certain approximations, one method to study a wide range of physically realizable EoSs is to parameterize them in a model-independent way. Spectral representations [18–22] parameterize EoSs by performing spectral expansions on the adiabatic index $\Gamma(p)$ ¹:

$$\Gamma(x) = \exp \sum_k \gamma_k x^k, \quad (1)$$

where $x \equiv \log p/p_0$ for minimum pressure p_0 . The equation of state is then determined by an integration of the differential equation:

$$\frac{d\epsilon(p)}{dp} = \frac{\epsilon(p) + p}{p\Gamma(p)}. \quad (2)$$

Using this formalism, any valid EoS can be approximated through choice of 4 or more spectral coefficients γ_k , tabulated for several common EoSs in Table 1 of [18].

In the current analysis, we consider EoSs which have been constrained by the recent binary neutron star merger event, GW170817. Important recent work [15] sampled EoS parameters in order to derive a marginalized posterior on the pressure as a function of mass density, as seen in Fig. 2 of [15]. The spectral coefficients were sampled within the ranges: $\gamma_0 \in [0.2, 2]$, $\gamma_1 \in [-1.6, 1.7]$, $\gamma_2 \in [-0.6, 0.6]$, $\gamma_3 \in [-0.02, 0.02]$, and further restricted the adiabatic index to be $\Gamma \in [0.6, 4.5]$, ensuring the parameterization exposed a wide range of viable EoSs [26]. Additional constraints imposed upon the generated EoSs

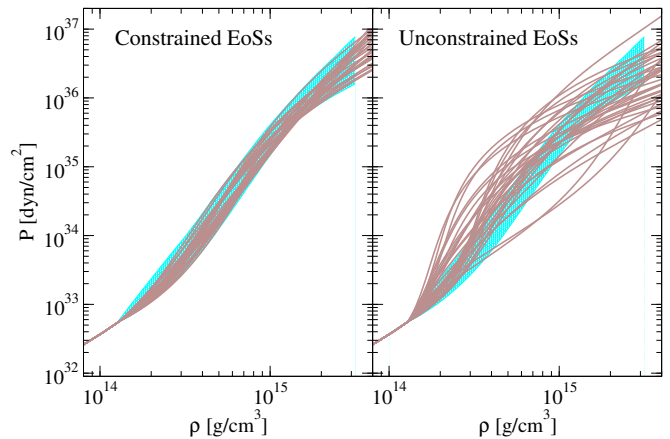


FIG. 2. Small representative sets of the constrained (left) and unconstrained (right) EoSs used in this analysis. The constrained EoSs were populated by randomly selecting 100 posterior samples obtained from the GW170817 90% credible level shown in cyan [15]. Additionally, 100 unconstrained EoSs were generated by randomly sampling spectral coefficients of physically valid EoSs, with no further constrained applied. The following constraints were also applied to both sets of EoSs: (i) the EoS must have a causal structure within 10%, and (ii) the EoS must support maximum NS mass of at least $1.97 M_\odot$, consistent with astrophysical observations. Finally, the high density core EoSs generated above were stitched to the low-density crust EoS of SLy [27] at $\rho_{\text{stitch}} = 1.3 \times 10^{14} \text{ g/cm}^3$.

were as follows [15]: (i) causality within 10%, and (ii) EoS priors must support NS masses up to $1.97 M_\odot$, consistent with astrophysical observations. We utilize a random set of 100 of the above posterior samples defined by GW170817, furthermore referenced as the “constrained EoSs”, as shown in Fig. 2. *zc: Carl, can you describe how you generated these? They aren’t the actual posteriors, are they?* Following [23], the parameterized high-density core EoSs generated above are matched to the low-density crust EoS Sly [27] at about half of the nuclear saturation density, $\rho_{\text{stitch}} = 1.3 \times 10^{14} \text{ g/cm}^3$. For comparison, we also include a second sample of 100 “unconstrained” EoSs, randomly sampled in the pressure-density plane to be unrestricted by GW170817s posterior.

In addition, we investigate 10 transitional quark-hadron matter stars, which undergo first-order phase transitions at pressure P_{tr} , where the hadronic branch departs into a quark-matter branch at a given mass transition [17, 28–31]. In particular, we focus on the ACS and ACB models described in Ref. [17], shown in Fig. 3. These result in two distinct types of NSs, based on their observed mass: (i) massive ($M \geq M_{\text{tr}}$) hybrid stars which have quark-matter cores and nuclear matter crusts (we denote this as “HS”), and (ii) small-mass ($M \leq M_{\text{tr}}$) hadronic stars with no internal transition to quark matter (we denote this as “NS”).

¹ Another way of parameterizing EoSs is the piecewise polytropic formulation [23–25].

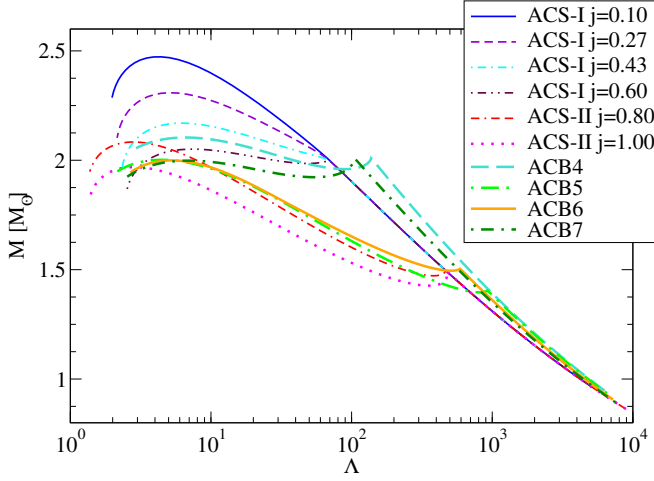


FIG. 3. $M-\Lambda$ relations for the ACS and ACB class model hybrid stars. Observe the transitional points where the NS transitions from the hadronic branch into a quark-matter branch. As described in the text, HS/HS and NS/NS binaries have individual masses chosen such that both stars are contained within one branch – resulting in high q values. Contrastingly, HS/NS binaries have individual masses chosen from each branch resulting in small q -values.

B. Neutron Star Tidal deformability

Binary neutron star mergers, such as GW170817, provide valuable insight into the internal structure of such stars. Namely, tidal effects which enter the gravitational waveform depend strongly on the EoS defining the NSs structure. The ($l = 2$ electric type) *tidal deformability*, denoted as λ , has the largest impact on the waveform phase. Consider a NS of mass M in the presence of the tidal field ε_{ij} of a companion star. In response, the NS will deform away from sphericity under the acquisition of quadrupole moment Q_{ij} , characterized by λ as the linear response to ε_{ij} [11, 12, 32]:

$$Q_{ij} = -\lambda \varepsilon_{ij}. \quad (3)$$

One can extract Q_{ij} and ε_{ij} – and thus λ , or its dimensionless form $\Lambda \equiv \lambda/M^5$ – via different asymptotic limits of the gravitational potential:

$$\begin{aligned} \Phi = \frac{1+g_{tt}}{2} = & -\frac{M}{r} - \frac{3}{2} \frac{Q_{ij}}{r^3} \left(\frac{x^i x^j}{r} - \frac{1}{3} \delta_{ij} \right) + \mathcal{O}\left(\frac{M^4}{r^4}\right) \\ & + \frac{1}{2} \varepsilon_{ij} x^i x^j + \mathcal{O}\left(\frac{r^3}{M^3}\right). \end{aligned} \quad (4)$$

The metric component g_{tt} is determined by first constructing a spherically symmetric, non-spinning background solution, followed by the introduction of a perturbative tidal deformation. Next, the perturbed Einstein equations must be solved in the NSs interior given

an EoS, then matched to the exterior Schwarzschild solution at the surface, modulo a constant. This process is described in more detail in Ref. [11]. Further, the stellar mass and radius are determined from $p(R) = 0$, and the above mentioned constant. Similarly, the moment of inertia is obtained from the asymptotic behavior of the $g_{t\phi}$ metric component.

Next, we consider the case of two NSs in a binary, such as the system found in GW170817, where each star individually experiences a neighboring tidal field. Thus each star possesses tidal deformabilities Λ_1 and Λ_2 entering the gravitational waveform. Due to strong correlations between these parameters, individual extraction is very difficult with current interferometer sensitivity limitations. However, the waveform templates can be strategically reparameterized to instead include independent linear combinations of Λ_1 and Λ_2 to mitigate correlations between them. Any set of two independent functions may be used, for example: tidal parameters $\tilde{\Lambda} = \tilde{\Lambda}(\Lambda_1, \Lambda_2)$ and $\delta\tilde{\Lambda} = \delta\tilde{\Lambda}(\Lambda_1, \Lambda_2)$ [33] first enter the gravitational waveform at 5PN and 6PN orders respectively, thus partially breaking degeneracies. Here, $\tilde{\Lambda}$ is known as the mass weighted tidal deformability, or *chirp deformability* due to its status as the dominant tidal parameter in the waveform.

C. EoS insensitive relations

Current gravitational wave interferometry is not yet sensitive enough to accurately extract both tidal parameters $\tilde{\Lambda}$ and $\delta\tilde{\Lambda}$. In a search to remedy this, important previous work by Yagi and Yunes [13] found that symmetric and antisymmetric combinations of tidal deformabilities:

$$\Lambda_s \equiv \frac{\Lambda_1 + \Lambda_2}{2}, \quad \Lambda_a \equiv \frac{\Lambda_1 - \Lambda_2}{2}, \quad (5)$$

display EoS-insensitive properties to a high degree, showing EoS variations up to 20% for binaries with masses less than $1.7 M_\odot$, for a representative set of 11 EoSs. These relations, known as “binary Love universal relations” allows one to break degeneracies between coupled tidal parameters. This is important for two reasons: (i) allows us to algebraically eliminate tidal parameters from the template parameter list, improving parameter estimation, and (ii) automatic measurement of second tidal parameter given observation of the first. It was shown through a simple Fisher analysis that the use of binary Love universal relations improved parameter extraction on $\tilde{\Lambda}$ by an order of magnitude.

Similar universal relations have been found to exist between individual NS observables: moment of inertia (I), tidal deformability (Love), and quadrupole moment (Q), known as the “I-Love-Q” universal relations [14]. These have been found to be EoS insensitive by up to 1% for each of pair of observables. In this paper, we show improvement in both of these universal relations by

restricting to EoSs sampled from GW170817s posterior on pressure as a function of density.

III. UNIVERSAL RELATIONS

In this section, we follow the analyses performed in [13, 14] with two new sets of 100 spectrally generated EoS: (i) posterior samples randomly selected from GW170817s 90% posterior on pressure as a function of density as shown in the left panel of Fig. 2, and (ii) those unconstrained by any prior EoS information, as shown in the right panel of Fig. 2.

A. I-Love-Q relations

Here we present our results on I-Love-Q universality as compared to Fig. 1 of Yagi and Yunes [14]. In particular, we consider two distinct classes of NSs: nuclear matter EoSs and hybrid quark-hadron star EoSs as described in Sec. II. We begin in Sec. III A 1 by fitting the new I-Love-Q universal relations using the constrained set of EoSs. This is followed in Sec. III A 2 by an analysis and discussion into how well hybrid stars agree with the improved binary Love relations.

1. Nuclear matter stars

Following the work of Ref. [14], the data for each universal relation is first fit to the following curve:

$$\ln y_i = a_i + b_i \ln x_i + c_i (\ln x_i)^2 + d_i (\ln x_i)^3 + e_i (\ln x_i)^4, \quad (6)$$

where the updated coefficients are given in Table I. Additionally, we offer an improvement to the functional form of the I-Love-Q fitting curve. Namely, we use the Newtonian relationships between various observables as a controlling factor in the fit [14]:

$$\bar{I}^N = C_{I\Lambda} \Lambda^{2/5}, \quad \bar{Q}^N = C_{Q\Lambda} \Lambda^{1/5}, \quad \bar{I}^N = C_{I\bar{Q}} \bar{Q}^2. \quad (7)$$

This is appended to an expansion in $\Lambda^{-1/5} \propto C$ (or $\bar{Q}^{-1/5}$), where $C = M/R$ is the compactness of the star. This results in the following overall fitting relation:

$$y = C_{yx} x^\alpha \frac{1 + \sum_{i=1}^3 a_i x^{-i/5}}{1 + \sum_{i=1}^3 b_i x^{-i/5}}, \quad (8)$$

where y and x correspond to NS observables \bar{I} , \bar{Q} , and Λ , and α is given by $2/5$, $1/5$, and 2 for the $\bar{I}-\Lambda$, $\bar{Q}-\Lambda$, and $\bar{I}-\bar{Q}$ relations, respectively. The new fitting coefficients are presented in Table II. While the two above fits both result in fits with similar R^2 values of ~ 0.9999995 for the data presented, the latter one has the advantage that it properly limits to the Newtonian case as $\Lambda \rightarrow \infty$ [13].

Fig. 4 shows the improved I-Love universal relations between the dimensionless moment of inertia $\bar{I} \equiv I/M^3$,

the dimensionless quadrupole moment $\bar{Q} \equiv Q/M^3$, and the dimensionless tidal deformability Λ for both the constrained and unconstrained sets of EoSs (each with individual fits pertaining to only that set of EoSs). We observe that the constrained EoSs show considerable improvement from both the results of previous works [14], and from the unconstrained EoSs. This is further validated in Tab. III, where the maximal EoS variation from each fit is tabulated; comparing the results of previous works to the unconstrained, and constrained sets of EoSs. Observe how the constrained EoSs outperform both other cases by a considerable amount for each I-Love-Q universal relation.

These results indicate that universal relations can indeed be greatly improved upon by constraining to only EoSs which agree with physical observations. In addition, we confirm the validity of this method by noting that the unconstrained EoSs observe more EoS variability than that found in Ref [14] due to the nature of large random sampling taking into account more sources of uncertainty than previously studied. On the other hand, the constrained set of EoSs show significant improvement from that found in previous works.

2. Hybrid quark-hadron stars

In this section, we investigate the I-Love-Q universality of hybrid stars, and their compatibility with the nuclear matter counterparts. We consider three different sets of data to be fit to Eq. 8:

1. Complete set of 100 constrained EoSs combined with the 10 hybrid star EoSs,
2. Complete set of 100 constrained EoSs alone,
3. Complete set of 10 hybrid star EoSs alone.

Following this, we compute the fractional difference from the fits for all three cases for the 10 hybrid star EoSs. The fractional differences for the second case fit (fit to only the constrained EoSs) is shown by the dashed green lines in Fig. 4 for example. To compare the three different fits, Tab. IV displays the maximal EoS variation in the $I-\Lambda$ relation for both the constrained and hybrid star EoSs in each case.

Observe how the hybrid star EoSs do obey the I-Love-Q universal relations up to $\sim 1.7\%$, slightly higher than that found here for nuclear matter EoSs, as well as that found in previous works [14]. Further, we observe that the universality can not be improved by much through the introduction of new fits, only bringing the max EoS variation down to $\sim 1\%$ for the fits constructed with only hybrid star EoSs. Concluding, we claim that hybrid star EoSs *do* obey the I-Love-Q universal relations computed through nuclear EoS data, with the exception that the universality goes up to $\sim 1.7\%$.

TABLE I. Updated fit parameters for the I-Love-Q universal relations, fitted to the constrained EoS data by the curve found in Eq. 6.

y_i	x_i	a_i	b_i	c_i	d_i	e_i
\bar{I}	Λ	1.4934168	0.0640972	0.0208513	-5.018022×10^{-4}	3.1638958×10^{-7}
\bar{Q}	Λ	0.2092931	0.0740442	-0.0538210	-5.018022×10^{-3}	1.576165×10^{-4}
\bar{I}	\bar{Q}	1.3832702	0.05931020	-0.0216132	0.0419044	$-2.9676365 \times 10^{-3}$

TABLE II. I-Love-Q universal relations fit parameters for the constrained EoS data using the improved fitting relations found in Eq. 8. This fitting relation, unlike previous versions, properly limits to the Newtonian case as $\Lambda \rightarrow \infty$.

y	x	α	C_{yx}	a_1	a_2	a_3	b_1	b_2	b_3
\bar{I}	Λ	2/5	0.5313031	1.2868285	0.0988787	-2.3001034	-1.3465945	0.3857349	-0.0287014
\bar{Q}	Λ	1/5	3.5554627	-2.1218079	2.7237378	-1.4906808	0.8643535	-0.1427541	-1.3973147
\bar{I}	\bar{Q}	2	0.0089212	10.5910815	-37.4581345	43.1831156	-2.3610288	1.9674667	-0.5678018

TABLE III. Comparison between the universal relations (both I-Love-Q and binary Love) maximal EoS variability for the results of previous works [13, 14], and the unconstrained and constrained sets of EoSs analyzed here. The maximum EoS variation, given by the largest fractional difference from the fits as shown in Figs. 4 and 5, sees a considerable improvement for the constrained set of EoSs, compared to the unconstrained set as well as previous works. Additionally, notice how the maximal EoS variation for the unconstrained set of EoSs is slightly higher than that found in Refs. [13, 14] - due to the effects of large random sampling taking into account more sources of uncertainty.*zc: Kent do you know the IQ max EoS variation? It's not quoted or shown in the paper*

Universal Relation	Maximal EoS Variability		
	Previous	Unconstrained	Constrained
$\bar{I} - \Lambda$	~ 0.005	0.0076725	0.0031383
$\bar{Q} - \Lambda$	~ 0.009	0.012617	0.0046612
$\bar{I} - \bar{Q}$?	0.014895	0.0057157
$\Lambda_a - \Lambda_s$ ($q = 0.90$)	~ 0.50	0.5723891	0.2140192
$\Lambda_a - \Lambda_s$ ($q = 0.7$)	~ 0.20	0.2447418	0.0828446
$\Lambda_a - \Lambda_s$ ($q = 0.50$)	~ 0.025	0.0384088	0.0182308

B. Binary love relations

Next we consider improvements to the binary Love universal relations. Similar to Sec. III A, we consider two classes of NSs: nuclear matter EoSs and hybrid quark-hadron star EoSs [17, 28–31]. We begin in Sec. III B 1 by fitting new binary Love relations for nucleonic matter as was done in [13]. This is followed in Sec. III B 2 by an analysis and discussion into different fits incorporating hybrid star EoSs.

TABLE IV. Comparison between the $\bar{I} - \Lambda$ maximal EoS variability for the constrained EoSs and the hybrid EoSs for three different cases of fitting data to Eq. 8: (1) fit to the combined data of constrained and hybrid EoS, (2) fit to the constrained EoS data alone, and (3) fit to the hybrid EoS data alone. Observe how for all 3 cases, the hybrid EoSs are only universal up to a minimum of $\sim 1\%$, while in each case the constrained EoSs outperform the hybrid ones. The second case is demonstrated in Fig. 4.

Fitting Case	Maximal EoS Variability	
	Constrained	Hybrid
Combined (Case 1)	0.0044066	0.0136338
Constrained only (Case 2)	0.0031383	0.0173574
Hybrid only (Case 3)	0.0084002	0.0101741

1. Nuclear matter stars

Following Ref. [13], we fit the binary Love relations from the constrained EoSs to the two-dimensional curve:

$$\Lambda_a = F_n(q) \frac{1 + \sum_{i=1}^3 \sum_{j=1}^2 b_{ij} q^j x^{i/5}}{1 + \sum_{i=1}^3 \sum_{j=1}^2 c_{ij} q^j x^{i/5}} \Lambda_s^\alpha, \quad (9)$$

where q is the mass ratio $q \equiv m_1/m_2$ with $m_1 \leq m_2$, and $F_n(q)$ being the Newtonian limit given by:

$$F_n(q) \equiv \frac{1 - q^{10/(3-n)}}{1 + q^{10/(3-n)}}. \quad (10)$$

The updated fit parameters can be found in Table V. Notice how, unlike the individual NS I-Love-Q universal relations, these relations also depend on the ratio of constituent masses in the binary system.

Fig. 5 shows the improved binary Love universal relation for 3 different mass ratios: $q = 0.9$, $q = 0.75$, and $q = 0.5$ for both constrained and unconstrained sets of EoSs. Observe how once again, the constrained set of EoSs show a considerable improvement upon both the

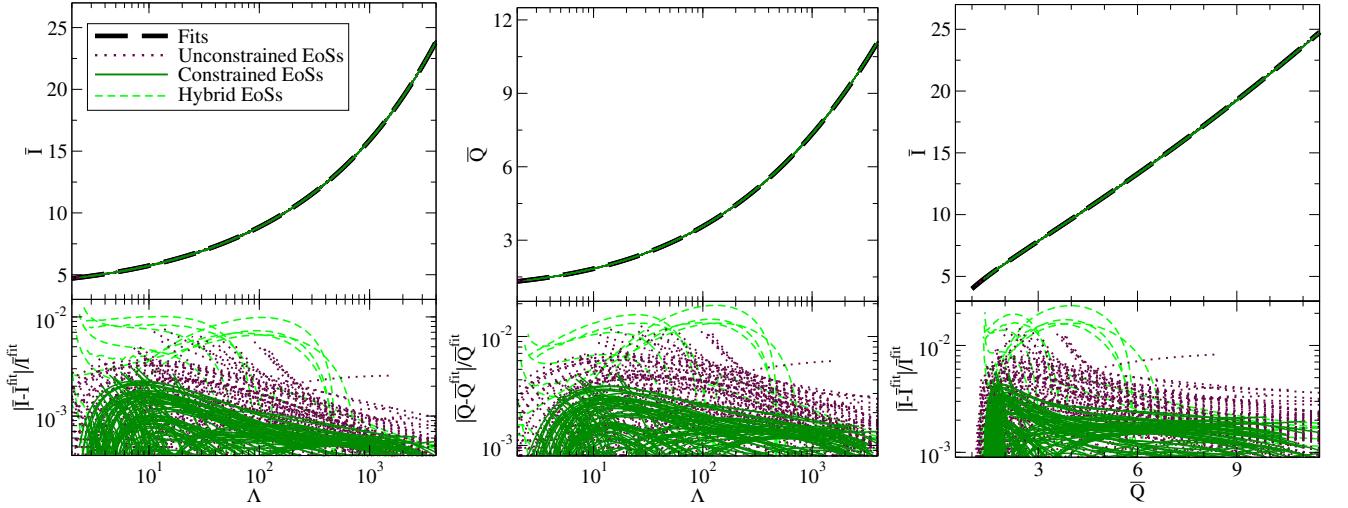


FIG. 4. Individual I-Love universal relations $\bar{I} - \Lambda$ (left), $\bar{Q} - \Lambda$ (center), and $\bar{I} - \bar{Q}$ (right), shown for both the constrained EoSs (solid green) and unconstrained EoSs (dotted maroon). In these figures, the black dashed lines corresponds to the fits given by Eq. 8 (note: each panel contains individual fits for the constrained and unconstrained EoSs, indistinguishable on such a large scale). Observe how the fractional difference from the fits, shown in the bottom panels, is greatly suppressed for the constrained case, compared to both the unconstrained case, and results from previous works [14]. The maximal EoS variation from the fits for the unconstrained and constrained sets of EoSs are compared in Tab. III. Additionally shown in this figure is the fractional difference from the nuclear matter fits for the 10 hybrid star EoSs (dashed green).

TABLE V. Updated fit parameters for the binary Love universal relations, as given by the curve found in Eq. 9. The bottom row corresponds to separate fits corresponding to the hybrid star branch of the hybrid EoSs.

Fit	n	α	b_{11}	b_{12}	b_{21}	b_{22}	b_{31}	b_{32}
NS	0.743	-1	-14.3953859	14.4524099	31.3639705	-32.2487464	-22.4377209	20.3458458
HS	0.743	-1	343.0432419	-382.6204995	519.4578954	-594.3272852	811.6275273	-867.6333691
			c_{11}	c_{12}	c_{21}	c_{22}	c_{31}	c_{32}
NS			-15.2461132	15.3712170	37.3335552	-43.1985996	-29.9331083	35.1806737
HS			82.5971248	-97.7858530	242.2411803	-262.9050666	244.8665753	-268.8024651

unconstrained set of EoSs, as well as the results found in previous works [13]. Additionally, the unconstrained set of EoSs show similar, yet slightly larger EoS variation due to the random sampling. Once again, the maximum EoS variability is tabulated in Tab. III for each value of mass ratio.

2. Hybrid quark-hadron stars

As described in Sec. II, transitional quark-hadron matter stars undergo first-order phase transitions at pressure P_{tr} , where the hadronic branch departs into a quark-matter branch at a given mass transition. These transitions result in two distinct types of NSs, based on their observed mass: (i) massive ($M \geq M_{\text{tr}}$) hybrid stars which have quark-matter cores and nuclear matter crusts (we denote this as “HS”), and (ii) small-mass ($M \leq M_{\text{tr}}$) hadronic stars with no internal transition to quark matter (we denote this as “NS”). We consider 3 classes of binaries:

- HS/NS binary: consists of one massive hybrid star, and one small hadronic neutron star,
- NS/NS binary: consists of two small-mass hadronic neutron stars,
- HS/HS binary: consists of two massive hybrid stars.

To determine how each of class of binary NSs obey our improved binary Love universal relations, we pick a representative set of 10 binary pairs from each class, for the ACB5 hybrid EoS, with a transition at $1.4 M_{\odot}$. Binary Love values are then computed for each pair, then residuals from the binary Love curve found in Sec. IIIB 1 are determined and compared to that from the constrained set of EoSs. The results are shown in Fig. 6. First, we observe that the NS/NS combination of stars gives consistent results to that found earlier – as expected. Next, we see that HS/HS combinations agree moderately with

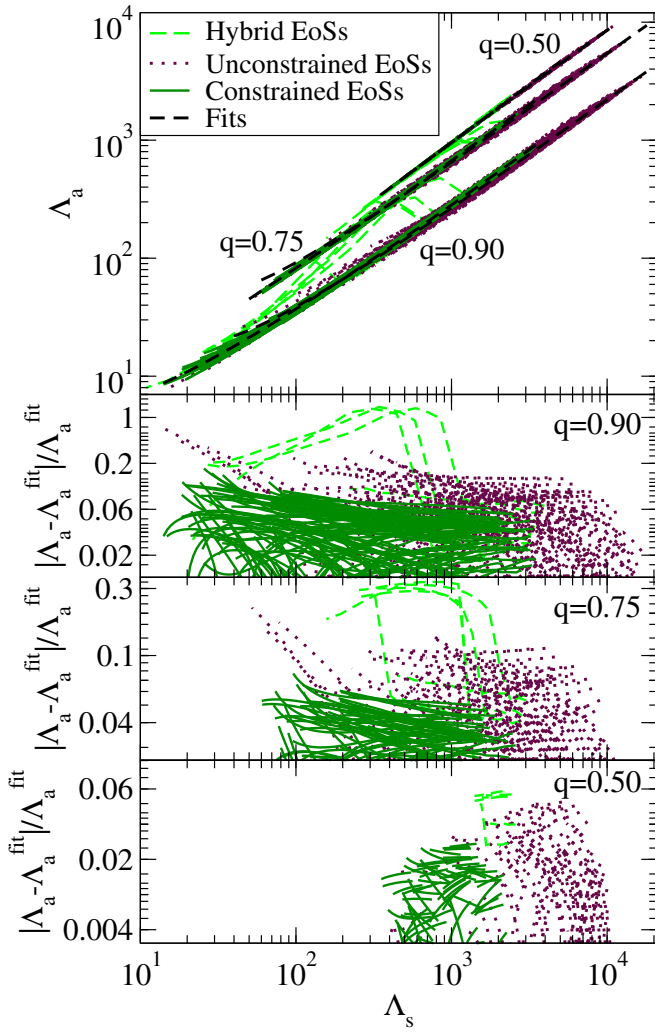


FIG. 5. Binary Love universal relations shown for the constrained EoSs (dotted maroon) and unconstrained EoSs (solid green) for various values of mass ratio: $q = 0.9$, $q = 0.75$, and $q = 0.50$. In this figure, the top panel displays the universal relations with fits given by Eq. 9 shown by dashed black lines, while the bottom 3 panels correspond to the EoS variation for each mass ratio. Observe how the constrained set of EoSs show a reduction in EoS variation for both the unconstrained set, and from the results shown in Ref. [13]. The max EoS variability for each case is tabulated and compared in Tab. III. Additionally shown is the binary Love relations for the 10 hybrid star EoSs (dashed green curves) as discussed in Sec. III B 2. Observe the large deviations from the fit as the mass ratio q increases, returning near the fit before the transitional pressure at large values of Λ_s .

previous relations², while HS/NS combinations disagree significantly. This can be explained by the large reduc-

² Note that these EoSs do not fit within GW170817s 90% posterior on EoS - so we expect deviations consistent with the “unconstrained” set of EoSs, rather than the “constrained” set.

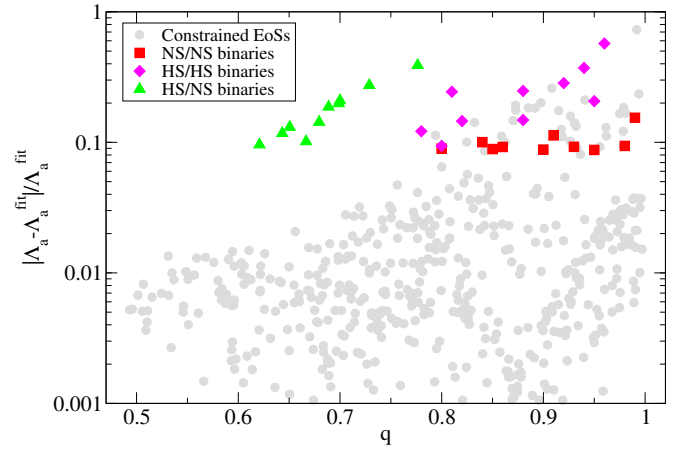


FIG. 6. Fractional difference from the improved binary Love relations fit for a representative set of constrained nuclear matter EoSs (gray circles), and 30 selected NS binaries from the ACB5 hybrid EoS. In particular, these binary pairs are selected from each of the following categories: (i) binaries with which one massive star has a quark matter core, while the other is pure hadronic matter (i.e. small enough mass that the transition point has not yet been reached), denoted HS/NS (green triangles); (ii) binary with both small-mass hadron stars, denoted NS/NS (red squares); and (iii) binary with both large-mass stars with quark matter cores, denoted HS/HS (magenta diamonds).

tion in tidal deformability for hybrid stars, are shown in Fig. 2 of Ref. [17]: when one star lies on the hadronic branch while the other is on the quark branch, they each see vast differences in $\tilde{\Lambda}$ - disrupting the binary Love relations as found for stars on the hadronic branch.

This discrepancy between hybrid and hadronic matter EoSs can be seen in Fig. 5, where the binary Love relations for the 10 hybrid star EoSs are shown in relation to the constrained and unconstrained nuclear matter EoSs. Observe how the residuals from the fit are quite good for low pressures (large Λ_s) when the binaries consist of a NS/NS combination, before reaching the transitional pressure when the deviations become increasingly large ($\sim 160\%$ for $q = 0.90$, $\sim 37\%$ for $q = 0.75$, and $\sim 6\%$ for $q = 0.50$) for HS/HS and HS/NS binaries.

To further investigate this phenomena, we consider binary Love fits to the HS branches, or NS branches *individually*. It was found that by trying to fit binary Love relations to the full hybrid star EoSs failed, due to the difference in transitional masses M_{tr} . To compensate for these differences, we separate the two branches into the NS (hadronic matter) and HS (hybrid matter) branches. We first observe that the NS branch obeys the “hadronic” binary Love relations derived earlier in Sec. III B 1 within the variability found earlier, indicating no further need for additional fits. However, the HS branch does not, suggesting the need for a new “hybrid” binary love fit pertaining to this branch. We begin by fitting the binary Love relations to the new HS branch, resulting in

the fit coefficients found in the bottom row of Tab. V. We urge caution with the use of these fits, as the small sample size (10 EoSs) as well as the occurrence of hybrid matter transitions only being available for certain mass ratios on certain EoSs, results in a less accurate fit than the nuclear-matter counterpart. Similar to before, the fractional difference from the fit for each HS branch is computed, resulting in a maximum variability of 18.488% for $q = 0.90$. This result is strongly consistent with the results found for the nuclear matter fits of Sec. IIIB 1.

We conclude this section with the observation that the hybrid star EoSs do *not* conform to the fits performed on nuclear matter EoSs. This is not surprising, as the hybrid branch of the EoSs give inconsistent results between Λ_1 and Λ_2 with different masses; an issue not present for the single-star I-Love-Q relations. By separating the two branches of the hybrid EoSs, we find a new “hybrid” branch binary Love fit which gives consistent results to that found for the nuclear matter fits.

3. Error Marginalization

We have now shown that binary NS merger observations can help improve universal relations - the question is: is it worth it? Current interferometer sensitivities are not yet small enough to accurately constrain $\tilde{\Lambda}$. For example, GW170817 was detected by LIGO observing run 2 (“O2”) **zc: cite** and was able to constrain $\tilde{\Lambda}$ to a 90% confidence interval of 325 (this relates to a standard deviation of $\sigma_{\tilde{\Lambda}} = 198$) centered at $\tilde{\Lambda} = 395$. This corresponds to statistical uncertainties on the order of $\sim 82\%$, which vastly dominates the error budget compared to the small systematic errors picked up by EoS variation in the universal relations, which can be seen in Fig. 7. This implies that currently, improved universal relations will only make a negligible difference in tidal parameter extraction.

In this section, we investigate the residuals in $\tilde{\Lambda}(\Lambda_a, \Lambda_s, q)$ in order to marginalize over the intrinsic error in the binary Love universal relations. In particular, we restrict our focus to only the constrained set of EoSs. Residuals in $\tilde{\Lambda}$ are computed as $\tilde{\Lambda}^{\text{fit}} - \tilde{\Lambda}^{\text{true}}$, where $\tilde{\Lambda}^{\text{true}} = \tilde{\Lambda}(\Lambda_a, \Lambda_s, q)$ corresponds to the true value predicted by the sample EoSs, and $\tilde{\Lambda}^{\text{fit}} = \tilde{\Lambda}(\Lambda_a^{\text{fit}}(\Lambda_s, q), \Lambda_s, q)$ corresponds to the value obtained through the universal relations found in Sec. IIIB 1. Following Ref. [34], we assume the residuals in $\tilde{\Lambda}$ observe a Gaussian distribution with mean and standard deviation given by:

$$\mu_{\tilde{\Lambda}}(\Lambda_s, q) = \frac{\mu_{\Lambda_s}(\Lambda_s) + \mu_q(q)}{2}, \quad (11)$$

$$\sigma_{\tilde{\Lambda}} = \sqrt{\sigma_{\Lambda_s}^2(\Lambda_s) + \sigma_q^2(q)}. \quad (12)$$

Similar to Ref. [34], we fit the individual components to be:

$$\mu_{\Lambda_s}(x) = \mu_1 x + \mu_2, \quad (13)$$

TABLE VI. Coefficients to the fits given by Eqs. (13)-(16) for the relative error on $\tilde{\Lambda}$ in the improved binary Love universal relations presented in this paper.

μ_1	$-8.7169662 \times 10^{-5}$	σ_1	$3.3497867 \times 10^{-11}$
μ_2	0.0185324	σ_2	$-2.3026166 \times 10^{-7}$
μ_3	-3.2611497	σ_3	3.8180750×10^{-4}
μ_4	5.0680859	σ_4	0.0444373
μ_5	-1.9040182	σ_5	-0.0126140
		σ_6	181.8712429
		σ_7	-419.0842028
		σ_8	299.5608266
		σ_9	-62.1555049

$$\mu_q(x) = \mu_3 x^2 + \mu_4 x + \mu_5, \quad (14)$$

$$\sigma_{\Lambda_s}(x) = \sigma_1 x^{7/2} + \sigma_2 x^{5/2} + \sigma_3 x^{3/2} + \sigma_4 x^{1/2} + \sigma_5, \quad (15)$$

$$\sigma_q(x) = \sigma_6 x^3 + \sigma_7 x^2 + \sigma_8 x + \sigma_9. \quad (16)$$

The fitting parameters μ_i and σ_i are tabulated in Table VI.

Figure 7 displays the Gaussian distribution of $\tilde{\Lambda}$ residuals for both the constrained, and unconstrained sets of EoSs for comparison. Observe how the standard deviations $\sigma = 7.666$ and $\sigma = 40.887$ show a large decrease between the unconstrained and constrained sets of EoSs. In addition, we find the 90th, 99th, and 100th percentiles on $\tilde{\Lambda}$ to be $P_{90} = 12.014$, $P_{99} = 29.710$, and $P_{100} = 62.240$ for the constrained EoSs. Because the un-binned residuals seen in Fig. 7 are dominated by the low-error regions of parameter space ($\Lambda_s \rightarrow 0$ and $q \rightarrow 1$) shown by the fits of Tab. VI, we consider the 90th for the remainder of the analysis. We take this value of $P_{90} = 12.014$ to be the systematic measurement error introduced by using the improved binary Love universal relations on the parameter extraction of $\tilde{\Lambda}$. Currently, the statistical error of 198 on $\tilde{\Lambda}$ from GW170817 dominate the error budget compared to the systematic error of 12.014. This means that, for the current “O2” detector sensitivity, the use of improved binary Love universal relations will only make a negligible difference on the extraction of $\tilde{\Lambda}$. However, future detectors (for example aLIGO, a++, Voyager, CE, and ET) are planned with large reductions in sensitivity - both decreasing the statistical errors and allowing for a larger binary NS merger detection rate; further reducing uncertainties. In Sec. IV, we analyze this further and discuss when the systematic errors from universal relations become comparable to the statistical errors.

IV. IMPACT ON FUTURE OBSERVATIONS

In this section, we estimate the feasibility of utilizing improved universal relations in future binary NS merger events. This estimate is acquired through a simple Fisher analysis [35, 36] which approximates the accuracy with which one can extract best-fit parameters θ^a , given a

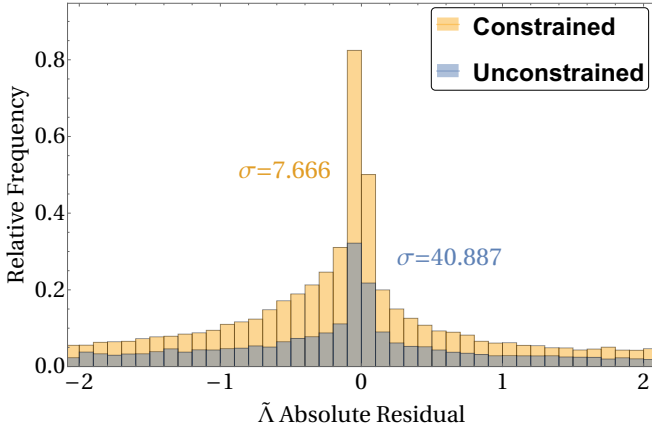


FIG. 7. Residuals on $\tilde{\Lambda}$ computed as $\tilde{\Lambda}^{\text{fit}} - \tilde{\Lambda}^{\text{true}}$ for the binary Love relations modeled in Sec. III B 1 for both constrained and unconstrained sets of EoSs. These residuals obey Gaussian distributions centered at $\mu = -1.8133 \times 10^{-4}$ and $\mu = 4.2258 \times 10^{-3}$ with standard deviations of $\sigma = 7.6664$ and $\sigma = 40.8866$ for the constrained and unconstrained sets of EoSs, respectively. These uncertainties correspond roughly to the systematic errors introduced on the parameter extraction of $\tilde{\Lambda}$ upon the use of binary Love universal relations. However, to take into account the systematic errors found in high-error regions of the parameter space, we instead set the systematic error to be the 90th percentile, $P_{90} = 12.014$. Observe that the systematic errors from using the improved (constrained) binary Love universal relations are negligible compared to the statistical errors accrued on parameter extraction from GW170817, found to be $\sigma_{\tilde{\Lambda}} = 198$.

prior template waveform. For the remainder of the paper, we consider a template parameter vector consisting of:

$$\theta^a = (\ln A, \phi_c, t_c, \ln \mathcal{M}, \ln \eta, \chi_s, \chi_a, \tilde{\Lambda}, \delta\tilde{\Lambda}), \quad (17)$$

where $A \equiv \sqrt{\frac{2\eta}{3\pi^{1/3}}}$ is a normalized amplitude factor, $\eta \equiv m_1 m_2 / M^2$ is the symmetric mass ratio with $m_{1,2}$ and M being the individual and total masses, $\mathcal{M} = M\eta^{3/5}$ is the chirp mass, and $\chi_{s,a} = \frac{1}{2}(\chi_1 \pm \chi_2)$ are the symmetric and antisymmetric total spins, where $\chi_{1,2}$ are the NSs individual spins. Following Refs. [36–38], this method relies on the crude assumption of Gaussian prior distributions³. The resulting posterior distribution is Gaussian with root-mean-square given by:

$$\Delta\theta^a = \sqrt{(\tilde{\Gamma}^{-1})^{aa}}. \quad (18)$$

Here, the Fisher matrix $\tilde{\Gamma}$ is defined by:

$$\tilde{\Gamma}_{ab} \equiv \left(\frac{\partial h}{\partial \theta^a} \middle| \frac{\partial h}{\partial \theta^b} \right) + \frac{1}{\sigma_{\theta^a}^2} \delta_{ab} \quad (19)$$

³ Typically, the more valid assumption is a uniform prior distribution; an improvement made in a more detailed Bayesian analysis.

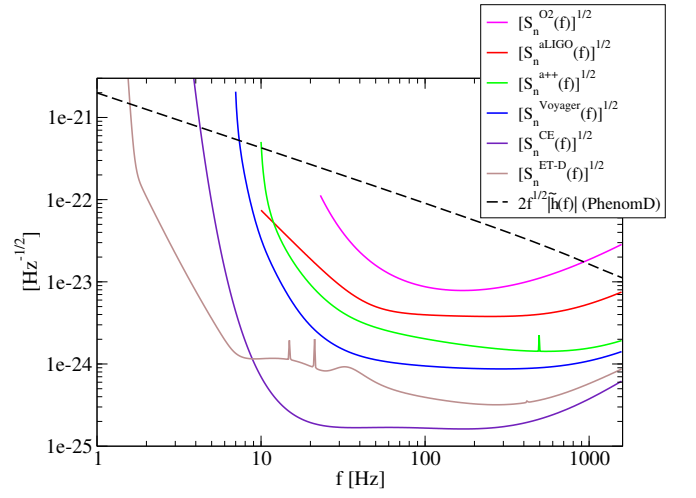


FIG. 8. Square root of the spectral noise densities $\sqrt{S_n^A(f)}$ plotted for detectors (A): LIGO O2 (orange), aLIGO (green), a++ (purple), Voyager (magenta), CE (red), and ET-D (blue) as interpolated from publicly available data^{zc: cite}. Spectral noise densities are plotted from $f_{\text{min}} = (23, 10, 10, 7, 1, 1)$ Hz, respectively, to $f_{\text{max}} = 1649$ Hz. Also shown is $2\sqrt{f}$ multiplied by the amplitude of the PhenomD [39, 40] waveform template, modified by tidal corrections from Ref. [33] used in our Fisher Analysis.

where h is the waveform template, σ_{θ^a} is the parameters' prior root-mean-square estimate, and the inner product is defined by:

$$(a|b) \equiv 2 \int_0^\infty \frac{\tilde{a}^* \tilde{b} + \tilde{b}^* \tilde{a}}{S_n(f)} df. \quad (20)$$

In this analysis, we consider the “PhenomD” waveform template [39, 40] modified by tidal corrections shown in Ref. [33]. Lastly, $S_n(f)$ is the spectral noise density for the given interferometer.

We begin by authenticating this approach by applying a Fisher analysis to GW170817, as observed by LIGO with O2 detector sensitivity^{zc: cite}. Further, we scale the luminosity distance such that the signal-to-noise-ratio ($SNR \equiv \rho$) is fixed to be $\rho = 32.4$, as was found in GW170817. We also assume low spin priors $|\chi| \leq 0.05$, as well as $\tilde{\Lambda} \leq 3000$ and $|\delta\tilde{\Lambda}| \leq 500$ [41]. The resulting posterior distribution on $\tilde{\Lambda}$ has a range of ± 276.99 encompassing the 90% credible levels. We compare these results with the Bayesian analysis performed in Ref. [16, 42], finding close agreement with the resulting 90% credible region of $70 \leq \tilde{\Lambda} \leq 720$. This confirms the approximate validity of this method, allowing a continuation of this analysis for future detectors.

Next, we consider events identical to GW170817 detected on future design sensitivity upgrades and detectors $A \equiv (\text{O2}, \text{aLIGO}, \text{a++}, \text{Voyager}, \text{CE}, \text{ET-D})$ ^{zc: cite}, shown in Fig. 8, to determine if and when the statistical errors associated with parameter extraction of $\tilde{\Lambda}$ drop

below the systematic EoS variation errors from using binary Love universal relations. The process we use for each detector sensitivity $S_n^A(f)$ is as follows:

- Perform a Fisher analysis as outlined above using $S_n^A(f)$, while restricting the luminosity distance D_L such that $\rho_{\text{GW170817}}^{\text{O2}} = 32.4$ would be achieved on O2 sensitivity $S_n^{\text{O2}}(f)$. This results in SNR ρ_{GW170817}^A and statistical error $\sigma_{\text{GW170817}}^A$ accrued in the extraction of $\tilde{\Lambda}$ on detector A .
- Generate a population of N_A events corresponding to the expected binary NS merger detection rate for detector A , following the distribution $f = 3\rho_{\text{th}}^3/\rho^4$ [43, 44] with a network SNR threshold of $\rho_{\text{th}} = 8$. This is calculated for the upper, central, and lower limits of the local binary NS coalescence rate density $R = 1540^{+3200}_{-1220} \text{ Gpc}^{-3}\text{yr}^{-1}$ [45], giving the rates shown in the second column of Table VII.
- Compute the population standard deviation given by:

$$\frac{1}{(\sigma_N^A)^2} = \sum_i^{N_A} \frac{1}{(\sigma_i^A)^2}, \quad (21)$$

where σ_i^A is computed by the relations $\sigma_i^A \times \rho_i^A = \sigma_{\text{GW170817}}^A \times \rho_{\text{GW170817}}^A$.

The results are compiled in Table VII, and shown graphically in Fig. 1 where $\sigma_{\text{GW170817}}^A$ and σ_N^A are plotted as a function of ρ_{GW170817}^A (the SNR as if GW170817 were detected on future detector A) for 5 future detector sensitivities.

Concluding, we find that the Voyager, ET, and CE detectors all exhibit enough uncertainty reduction that the systematics on $\tilde{\Lambda}$ introduced from using improved universal relations (found to be 12.014) no longer become negligible in the error budget. This implies that the use and further improvement of universal relations is justified for future binary NS merger detections. Further, we investigate the dependence of the measurement accuracy of $\tilde{\Lambda}$ on the binary NS mass ratio q for fixed chirp mass $\mathcal{M} = 1.88 M_\odot$ in Appendix A.

V. CONCLUSION AND DISCUSSION

The recent GW observation of binary NS merger GW170817 placed constraints on the supranuclear matter EoS for NSs. We take advantage of this by generating a restricted set of spectral EoSs which agree with this observation to reduce uncertainties upon the extraction of tidal parameters from future GW events. Important previous work by Yagi and Yunes [13, 14] found EoS-insensitive universal relations between symmetric and antisymmetric combinations of NS tidal deformabilities, which aid in the extraction of said tidal parameters. We find an improvement upon these universal relations by a

factor of $\sim 59\%$ for stars with mass ratios of 0.75 by restricting to the EoS posterior samples from GW170817s 90% credible region on pressure as a function of density. Similarly, we find an increase in I-Love-Q universality by a factors of $\sim 50\%$. In addition, we find that binaries consisting of one massive hybrid quark-hadron star, and one small-mass hadron star do not obey these universal relations – explained by the large difference in $\tilde{\Lambda}$ displayed between the constituent stars. To improve on this, we construct new “hybrid matter binary Love relations”, applied to only the hybrid branches of the transitional EoSs. This results in EoS variability similar to that found for the nuclear matter fits. Further, we analyze the impact of this improvement for future binary NS merger detections, as the current detector sensitivity is not yet small enough to accurately constrain $\tilde{\Lambda}$ enough for universal relations to make a difference. We find that future interferometers Voyager, CE, and ET-D all experience statistical uncertainties upon the extraction of $\tilde{\Lambda}$ small enough to become comparable to the systematic errors injected through the use of improved universal relations (found to be 12.014), as depicted in Fig. 1 and Table VII. Finally, in Appendix A we investigate the effect of NS binary mass ratio q on the measurement accuracy of $\tilde{\Lambda}$. We find that second generation interferometers lose accuracy as one increases the mass ratio, while third generation detectors observe a large increase of accuracy due to the correlations between $\tilde{\Lambda}$ and $\delta\tilde{\Lambda}$. This indicates that the use and further improvement of universal relations is justified for future GW observations of binary NS merger events.

zc: Discuss with group on possible avenues of future work.

ACKNOWLEDGMENTS

K.Y. would like to acknowledge networking support by the COST Action GWverse CA16104.

Appendix A: Measurement accuracy as a function of binary mass ratio

In this appendix, we discuss the effects of the binary NS mass ratio on the measurement accuracy of $\tilde{\Lambda}$ for various interferometers. The left panel of Fig. 9 displays an approximation of the $\tilde{\Lambda}$ measurement accuracy as a function of increasing mass ratio q (for a fixed chirp mass of $\mathcal{M} = 1.88 M_\odot$ corresponding to GW170817), using the Fisher analysis techniques described in Sec. IV. We observe two points of interest about these trends: (i) the second generation detectors (O2, aLIGO, a++, and Voyager) typically become less accurate as the mass ratio approaches unity, (ii) the third generation detectors (CE and ET) observe the opposite behavior– a fast growth in accuracy as the mass ratio increases. For the remainder of this appendix, we attempt to explain the opposing

TABLE VII. Tabulated results for the estimated statistical errors on $\tilde{\Lambda}$ for the combined results of N_A detections corresponding to the estimated upper, central, and lower limits of the binary NS merger detection rate R . This is repeated for 5 future detector sensitivities: aLIGO, a++, Voyager, CE, and ET. Below, ρ_{GW170817}^A and $\sigma_{\text{GW170817}}^A$ correspond to the approximate SNR and $\sigma_{\tilde{\Lambda}}$ of GW170817 had it been observed by the future interferometer, and σ_N^A corresponds to the final uncertainty on $\tilde{\Lambda}$ after N_A detections on interferometer A . It can be seen here that the statistical errors on $\tilde{\Lambda}$ become comparable with the systematics (set to be $P_{90} = 12.014$) from using improved binary Love relations from Voyager and on, indicating when it may be safe to utilize new universal relations. Note the approximation for σ_N^A under the O2 detector sensitivity is left blank due to the singularity of the detected event. These results are shown graphically in Fig. 1.

Detectors (A)	GW170817		Multiple events					
	ρ_{GW170817}^A	$\sigma_{\text{GW170817}}^A$	N_A			σ_N^A		
			Low	Central	High	Low	Central	High
O2	32.40	168.40	–	–	–	–	–	–
aLIGO	90.74	75.44	23	112	344	117.022	42.89	24.27
a++	180.95	31.55	208	1004	3091	27.62	13.36	7.36
Voyager	428.89	16.69	3854	1.85×10^4	5.71×10^4	8.57	3.78	2.16
ET-D	2807.45	6.26	3.98×10^5	1.91×10^6	5.89×10^6	0.78	0.35	0.20
CE	1398.03	4.85	1.35×10^7	6.50×10^7	2.00×10^8	0.34	0.16	0.10

behaviors of the second and third generation interferometers on the extraction of $\tilde{\Lambda}$.

We begin by considering the correlations between individual template parameters and $\tilde{\Lambda}$, given in Eq. 17. A simple approximation on the amplitude of these correlations can be performed by assuming all other correlations are non-existing. Correlations between parameters $\tilde{\Lambda}$ and θ^a alone is achieved by setting all off-diagonal Fisher matrix elements to 0, except for the (i, j) components such that both i and j correspond to the $\tilde{\Lambda}$ and θ^a parameters. We follow this process for each parameter in turn, and display the results in Fig. 10 for each interferometer. This figure, showing only the relative differences between correlations of different parameters θ^a and $\tilde{\Lambda}$, reveals a few things. First, the coalescence time t_c is highly correlated with $\tilde{\Lambda}$ equally for each interferometer, an unsurprising fact due to the high 4PN order at which the parameter enters the waveform. Secondly, correlations with 6PN tidal parameter $\delta\tilde{\Lambda}$ shows high correlations with $\tilde{\Lambda}$ for only the third generation detectors. This can be explained by the high PN order at which $\delta\tilde{\Lambda}$ enters the waveform, an effect that only the most sensitive of detectors can probe.

Following this conclusion on the difference of correlations between tidal parameters $\tilde{\Lambda}$ and $\delta\tilde{\Lambda}$ for second and third generation detectors, we attempt to describe the opposing behaviors of measurement accuracy between the two. Shown in the center panel of Fig. 9, we approximate the measurement accuracy of $\tilde{\Lambda}$ with the correlations between $\delta\tilde{\Lambda}$ and $\tilde{\Lambda}$ removed, through a process similar to that described above. Notice how the trends between detector generations become more similar – implying that the correlations between tidal parameters may be the cause. This is confirmed by the right panel of Fig. 9 where all parameter correlations have been removed from the Fisher matrix. We see that this results in identical behaviors between all 6 representative interferometers, leading us to conclude that the discrepancy

between interferometers comes from the degeneracies between different parameters in the gravitational waveform, namely the 6PN tidal parameter $\delta\tilde{\Lambda}$ which is only detectable by the highly sensitive third generation detectors CE and ET.

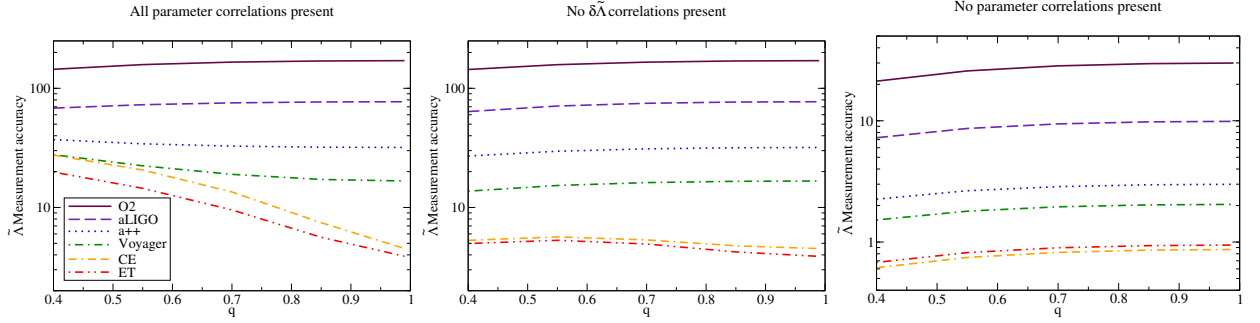


FIG. 9. Measurement accuracy of $\tilde{\Lambda}$ as a function of increasing mass ratio q for interferometer sensitivities O2, aLIGO, a++, Voyager, CE, and ET. Evaluated at a fixed chirp mass of $\mathcal{M} = 1.188 M_{\odot}$ corresponding to GW170817, this is repeated for three cases: (i) (left) with correlations between all template waveform parameters θ^a intact; (ii) (center) with the correlations between $\tilde{\Lambda}$ and $\delta\tilde{\Lambda}$ removed; and (iii) (right) with correlations between all parameters removed. The removal of parameter correlations is approximated by setting certain Fisher matrix elements to 0, as described in Appendix A. Observe how the left panel shows strong disagreement between second and third generation detectors, while the right panel shows identical behavior. This indicates that parameter correlations between $\tilde{\Lambda}$ and higher PN order parameter $\delta\tilde{\Lambda}$ to be the culprit in such a disagreement.

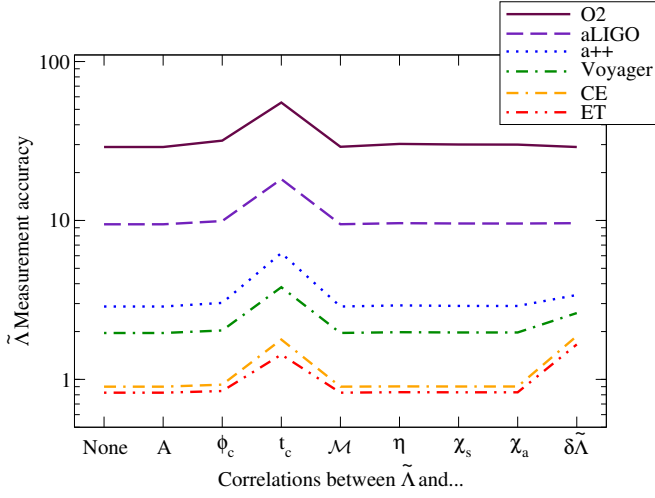


FIG. 10. Measurement accuracy of $\tilde{\Lambda}$ upon the consideration of correlations between *only* $\tilde{\Lambda}$ and other individual template parameters θ^a shown in Eq. 17. This process, repeated for 6 interferometer design sensitivities O2, aLIGO, a++, Voyager, CE, and ET, is approximated by setting all off-diagonal Fisher matrix elements to 0 except for the (i, j) components such that both i and j correspond to the $\tilde{\Lambda}$ and θ^a parameters. Observe how correlations with 4PN parameter t_c (coalescence time) remain to be highly correlated with $\tilde{\Lambda}$ among all 6 interferometers. However, correlations between 6PN tidal parameter $\delta\tilde{\Lambda}$ and $\tilde{\Lambda}$ only begin to make a strong impact for third generation detectors. This is due to the small effect that $\delta\tilde{\Lambda}$ has on the waveform, only to be distinguished by the most sensitive detectors.

-
- [1] B.-A. Li, L.-W. Chen, and C. M. Ko, *Physics Reports* **464**, 113 (2008).
 - [2] M. B. Tsang, Y. Zhang, P. Danielewicz, M. Famiano, Z. Li, W. G. Lynch, and A. W. Steiner, *Phys. Rev. Lett.* **102**, 122701 (2009).
 - [3] M. Centelles, X. Roca-Maza, X. Viñas, and M. Warda, *Phys. Rev. Lett.* **102**, 122502 (2009).
 - [4] B.-A. Li and L.-W. Chen, *Phys. Rev. C* **72**, 064611 (2005).
 - [5] L.-W. Chen, C. M. Ko, and B.-A. Li, *Phys. Rev. Lett.* **94**, 032701 (2005).
 - [6] T. Guver and F. Ozel, (2013), [arXiv:1301.0831 \[astro-ph.HE\]](#).
 - [7] F. Ozel, G. Baym, and T. Guver, *Phys. Rev. D* **82**, 101301 (2010), [arXiv:1002.3153 \[astro-ph.HE\]](#).
 - [8] A. W. Steiner, J. M. Lattimer, and E. F. Brown, *Astrophys. J.* **722**, 33 (2010).
 - [9] J. M. Lattimer and A. W. Steiner, *The European Physical Journal A* **50** (2014), 10.1140/epja/i2014-14040-y.
 - [10] F. Ozel and P. Freire, *Ann. Rev. Astron. Astrophys.* **54**, 401 (2016), [arXiv:1603.02698 \[astro-ph.HE\]](#).
 - [11] T. Hinderer, *The Astrophysical Journal* **677**, 1216 (2008).
 - [12] É. É. Flanagan and T. Hinderer, *Physical Review D* **77** (2008), 10.1103/physrevd.77.021502.
 - [13] K. Yagi and N. Yunes, *Classical and Quantum Gravity* **34**, 015006 (2017).
 - [14] K. Yagi and N. Yunes, *Phys. Rev. D* **88**, 023009 (2013).
 - [15] B. P. Abbott *et al.* (The LIGO Scientific Collaboration and the Virgo Collaboration), *Phys. Rev. Lett.* **121**, 161101 (2018).
 - [16] B. P. Abbott *et al.* (Virgo, LIGO Scientific), *Phys. Rev. Lett.* **119**, 161101 (2017), [arXiv:1710.05832 \[gr-qc\]](#).
 - [17] V. Paschalidis, K. Yagi, D. Alvarez-Castillo, D. B. Blaschke, and A. Sedrakian, *Physical Review D* **97** (2018), 10.1103/physrevd.97.084038.
 - [18] L. Lindblom, (2018), [arXiv:1804.04072 \[astro-ph.HE\]](#).
 - [19] L. Lindblom, *Phys. Rev. D* **82**, 103011 (2010), [arXiv:1009.0738 \[astro-ph.HE\]](#).
 - [20] L. Lindblom and N. M. Indik, *Phys. Rev. D* **86**, 084003 (2012), [arXiv:1207.3744 \[astro-ph.HE\]](#).
 - [21] L. Lindblom and N. M. Indik, *Phys. Rev. D* **89**, 064003 (2014), [Erratum: *Phys. Rev. D* **93**, no.12, 129903 (2016)], [arXiv:1310.0803 \[astro-ph.HE\]](#).
 - [22] B. P. Abbott *et al.* (Virgo, LIGO Scientific), (2018), [arXiv:1805.11581 \[gr-qc\]](#).
 - [23] J. S. Read, B. D. Lackey, B. J. Owen, and J. L. Friedman, *Physical Review D* **79** (2009), 10.1103/physrevd.79.124032.
 - [24] B. D. Lackey and L. Wade, *Phys. Rev. D* **91**, 043002 (2015), [arXiv:1410.8866 \[gr-qc\]](#).
 - [25] M. F. Carney, L. E. Wade, and B. S. Irwin, (2018), [arXiv:1805.11217 \[gr-qc\]](#).
 - [26] L. Lindblom and N. M. Indik, *Phys. Rev. D* **86**, 084003 (2012).
 - [27] F. Douchin and P. Haensel, *Astron. Astrophys.* **380**, 151 (2001), [arXiv:astro-ph/0111092 \[astro-ph\]](#).
 - [28] M. G. Alford and A. Sedrakian, *Phys. Rev. Lett.* **119**, 161104 (2017), [arXiv:1706.01592 \[astro-ph.HE\]](#).
 - [29] Z. F. Seidov, *Sov. Ast.* **15**, 347 (1971).
 - [30] J. L. Zdunik and P. Haensel, *Astron. Astrophys.* **551**, A61 (2013), [arXiv:1211.1231 \[astro-ph.SR\]](#).
 - [31] M. G. Alford, S. Han, and M. Prakash, *Phys. Rev. D* **88**, 083013 (2013), [arXiv:1302.4732 \[astro-ph.SR\]](#).
 - [32] K. Yagi and N. Yunes, *Physical Review D* **88** (2013), 10.1103/physrevd.88.023009.
 - [33] L. Wade, J. D. E. Creighton, E. Ochsner, B. D. Lackey, B. F. Farr, T. B. Littenberg, and V. Raymond, *Phys. Rev. D* **89**, 103012 (2014).
 - [34] K. Chatziioannou, C.-J. Haster, and A. Zimmerman, *Phys. Rev. D* **97**, 104036 (2018).
 - [35] L. S. Finn, *Phys. Rev. D* **46**, 5236 (1992).
 - [36] C. Cutler and E. E. Flanagan, *Phys. Rev. D* **49**, 2658 (1994).
 - [37] E. Berti, A. Buonanno, and C. M. Will, *Phys. Rev. D* **71**, 084025 (2005).
 - [38] E. Poisson and C. M. Will, *Phys. Rev. D* **52**, 848 (1995).
 - [39] S. Khan, S. Husa, M. Hannam, F. Ohme, M. Pürrer, X. J. Forteza, and A. Bohé, *Phys. Rev. D* **93**, 044007 (2016).
 - [40] S. Husa, S. Khan, M. Hannam, M. Pürrer, F. Ohme, X. J. Forteza, and A. Bohé, *Phys. Rev. D* **93**, 044006 (2016).
 - [41] L. Wade, J. D. E. Creighton, E. Ochsner, B. D. Lackey, B. F. Farr, T. B. Littenberg, and V. Raymond, *Phys. Rev. D* **89**, 103012 (2014).
 - [42] B. P. Abbott *et al.*, *Arxiv* (2018), 1805.11579v1.
 - [43] B. F. Schutz, *Classical and Quantum Gravity* **28**, 125023 (2011).
 - [44] H.-Y. Chen and D. E. Holz, (2014), [arXiv:1409.0522 \[gr-qc\]](#).
 - [45] B. Abbott *et al.*, *Physical Review Letters* **119** (2017), 10.1103/physrevlett.119.161101.